SCIENTIFIC REPORTS
nature research

OPEN

Simulating the human colorectal cancer microenvironment in 3D tumor-stroma co-cultures *in vitro* and *in vivo*

Mahesh Devarasetty[1], Anthony Dominijanni[1], Samuel Herberg[2], Ethan Shelkey[1], Aleksander Skardal[3] & Shay Soker[1]✉

The tumor microenvironment (TME) plays a significant role in cancer progression and thus modeling it will advance our understanding of cancer growth dynamics and response to therapies. Most *in vitro* models are not exposed to intact body physiology, and at the same time, fail to recapitulate the extensive features of the tumor stroma. Conversely, animal models do not accurately capture the human tumor architecture. We address these deficiencies with biofabricated colorectal cancer (CRC) tissue equivalents, which are built to replicate architectural features of biopsied CRC tissue. Our data shows that tumor-stroma co-cultures consisting of aligned extracellular matrix (ECM) fibers and ordered micro-architecture induced an epithelial phenotype in CRC cells while disordered ECM drove a mesenchymal phenotype, similar to well and poorly differentiated tumors, respectively. Importantly, co-cultures studied *in vitro*, and upon implantation in mice, revealed similar tumor growth dynamics and retention of architectural features for 28 days. Altogether, these results are the first demonstration of replicating human tumor ECM architecture in *ex vivo* and *in vivo* cultures.

Tumors are products of their environment. They send signals that can have significant effects on local tissue, and they receive signals from nearby cells and extracellular matrix (ECM) that can alter their progression[1–3]. Despite the importance of a tumor's environment, current strategies for prognostication of tumors are centered around analyses of the tumor cells in isolation, such as morphological assessment or proliferative index calculation[4,5]. Although these metrics are correlated to tumor progression, they do not capture the dynamics between a tumor and its surrounding space leading to inaccuracies when attempting to predict tumor progression and chemotherapeutic response[6,7]. New technologies that improve prognostication will have a significant effect on patient mortality and lead to development of novel therapeutics which target and control tumor cells specifically, sparing healthy tissue from the deleterious effects of contemporary chemotherapeutics[8,9].

Recent studies have identified the tumor microenvironment (TME) as a major contributing factor to cancer development and growth. The combination of paracrine factors, stromal cells such as endothelial, macrophages and tumor associated fibroblasts (TAFs), ECM proteins, and tissue mechanics coalesce into the perfect environment for a cancer to thrive and evade treatment[2,3]. Of particular interest to our research: a number of studies have shown that tissue biomechanics[10–12] and ECM architectures[13,14] can alter and guide cancer cell phenotype, as well as alter therapeutic response. These findings indicate the TME as a potential target for innovative anti-cancer cell, or cancer-modulating, therapies. To devise TME targeting therapies, *in vitro* models of the TME need to be developed and validated. Many groups, including ours, have used tissue engineering techniques to fabricate tumor constructs that replicate the unique combination of factors in the TME[15–21]. Tumor models can be prepared from human-derived cells with ECM proteins, yielding an accurate representation of the tumor-stroma interactions found in the TME, unlike many gold-standard animal cancer models. However, *in vitro* models typically cannot replicate the context of whole-body physiology to test side-effects or pharmacodynamics and pharmacokinetics since they are constructed to replicate single tissues[22–24].

Previously, we developed a three-dimensional (3D) model of the colonic submucosa complete with the unique micro-architecture found there[16]. When we embedded tumor spheroids composed of malignant colorectal cancer

[1]Wake Forest Baptist Medical Center, Winston-Salem, NC, 27101, USA. [2]SUNY Upstate Medical University, Syracuse, NY, 13210, USA. [3]The Ohio State University, Columbus, OH, 43210, USA. ✉e-mail: ssoker@wakehealth.edu

cells within these submucosal constructs, we found that the tumor cells behave radically different depending on the organization of the collagen ultrastructure. In ordered, organized TMEs, CRC cells exhibited behaviors akin to colonic epithelial cells with polarization and low proliferation rates. Interestingly, when placed into randomly assorted collagen I matrices, the CRC cells became highly motile and invasive with a high index of proliferation – in other words, they assumed a cancerous phenotype. Furthermore, structured ECM induced chemoresistance in CRC cells while randomly organized ECM caused chemosensitivity[16]. These results indicated that the presence of healthy stromal cells, capable of structuring the tumor ECM, has a suppressive effect on tumor cell phenotype and growth.

To further our understanding of ECM architecture and its role in modulating tumor growth, we analyzed CRC biopsies finding significant changes in ECM organization. Based upon our clinical observations, we fabricated CRC co-cultures containing CRC cells and hepatic stellate cells to replicate the stromal cell content and organization found in liver, the most common site of CRC metastasis[25]. We hypothesized that the presence of stromal cells in the TME will drive ECM organization and subsequently modulate CRC tumor growth in the model. To broaden the application of tumor co-cultures as an *ex-vivo* model of tumor growth, we implanted them subcutaneously in nude mice. We hypothesized that stromal cell-driven ECM architecture *ex vivo* will be preserved for an extended time *in vivo*. To test our hypotheses, we analyzed TME organizations and corresponding tumor cell phenotypes in co-cultures for 4 weeks *in vitro* and *in vivo* and found that samples with orderly structured stromal ECM, generated *in vitro*, maintained these structures *in vivo* throughout observation, and induced an epithelial phenotype in CRC cells. In contrast, disordered ECM allowed for mesenchymal phenotype. These results indicate that a pre-structured TME maintains its architecture in the context of whole-body physiology. Together, we present data on interactions between ECM architecture and cancer cell phenotype in three different systems, *in vitro*, in mice and in clinical samples. These findings demonstrate the clinical relevance of our CRC model and can be used as a model for studying tumor growth *ex-vivo* and prediction of potential response to chemotherapeutic drugs.

Results

Tumor tissue has a fewer collagen-rich areas and disorganized collagen architecture compared to normal colon tissue. We obtained colon tissue biopsies from 12 healthy, 6 well differentiated (low-grade), and 6 poorly differentiated (high-grade) CRC patients, and assessed the differences in the patterns of collagen-rich areas between healthy tumor tissues[26–28]. Trichrome staining of healthy tissue (Fig. 1a) shows distinct compartmentalization of collagen (blue signal) outside the crypt structures of the colon, and the collagen also appears striated and aligned within the submucosal layers. CRC tissue (Fig. 1b,c), conversely, shows less collagen overall, further decreasing from low grade to high grade, and the collagen becomes more dispersed with increasing grade. Due to the differences between tissue compartments, we divided the healthy and cancerous colon tissue into two distinct areas: the mucosa/crypt and the submucosa (Fig. 1d–f). To further characterize collagen fiber organization in these healthy colon and CRC specimens, we captured the birefringent collagen signal from picrosirius red (PSR)-stained sections corresponding to those areas (Fig. 1d–f **outsets**). PSR images demonstrate a similar pattern to trichrome: aligned and bundled collagen in healthy samples, and fibrillar, disordered collagen in diseased samples.

We digitally separated images described in Fig. 1d–f into the crypt or submucosa compartments while retaining the original tumor grade information. Then we performed automated fiber segmentation using CT-FIRE[29] to further quantify our observations of structural changes to collagen in CRC tissue dependent on grade. We pooled fiber measurements from all patients to reduce inter-patient variability and find global changes in grade-related fiber parameters. In the crypt compartments, we observed that collagen fibers (Fig. 2a) become significantly more random (angular analysis) and wider in specimen derived from low- and high-grade CRC patients compared with healthy tissue (Fig. 2b-**left and middle, respectively**), whereas the fiber length decreased only in high-grade CRC patient samples (Fig. 2b-**right**). Color of PSR signal indicates the bundling or maturity of collagen: red/orange signal corresponds to bundled and thickened fibers (mature) while yellow/green labels thin and reticular collagen (young or immature). To quantify the color, we performed hue analysis with a custom Matlab script. Hue analysis of birefringent signal showed no significant differences between any of the groups (Suppl. Fig. 12). This suggests that collagen reorganization over longer periods of time in adult tissue, may not significantly impact collagen maturation. In the submucosal compartments, we found that collagen fibers had narrower angular distribution in specimen from the cancerous tissues compared with healthy tissue (Fig. 2d-**left**). Fiber width decreased in specimen from healthy individuals to low-grade and further decreased in high-grade CRC specimen (Fig. 2d-**middle**). Fiber length was lower in specimen from low- and high-grade CRC patients compared to tissue from healthy individuals (Fig. 2d-**right**). Qualitative image analysis corroborated these results showing longer and wider fibers in the healthy specimen, and a higher density of short and thin fibers in the tumor specimen (Fig. 2c). Together, these results demonstrate that collagen fiber micro-architecture changes during cancer progression with different dynamics for each colon tissue region, the mucosa or submucosa.

Replicating native collagen architectures with bioengineered tumor co-cultures. To model the effects of collagen architecture on tumor phenotype, we produced tissue equivalent models with microenvironmental collagen architecture similar to human biopsies (outlined in Suppl. Fig. 1a)[16]. We embedded immortalized hepatic stellate cells (LX2) into a collagen I hydrogel which, in accordance with our previous studies[16], resulted in the active remodeling of collagen I and formation of structured and bundled fibers that resemble those observed in native tissue[30]. Stellate cells have been shown to support metastatic CRC growth and thus represent a relevant cell type for *in vitro* CRC models[31,32]. In parallel, we produced bare collagen constructs which would replicate the disorganized collagen features of high-grade CRC tumors[16]. To test if the co-culture and collagen only constructs can recapitulate the collagen organization features observed in healthy colon, low-, or high-grade CRC,

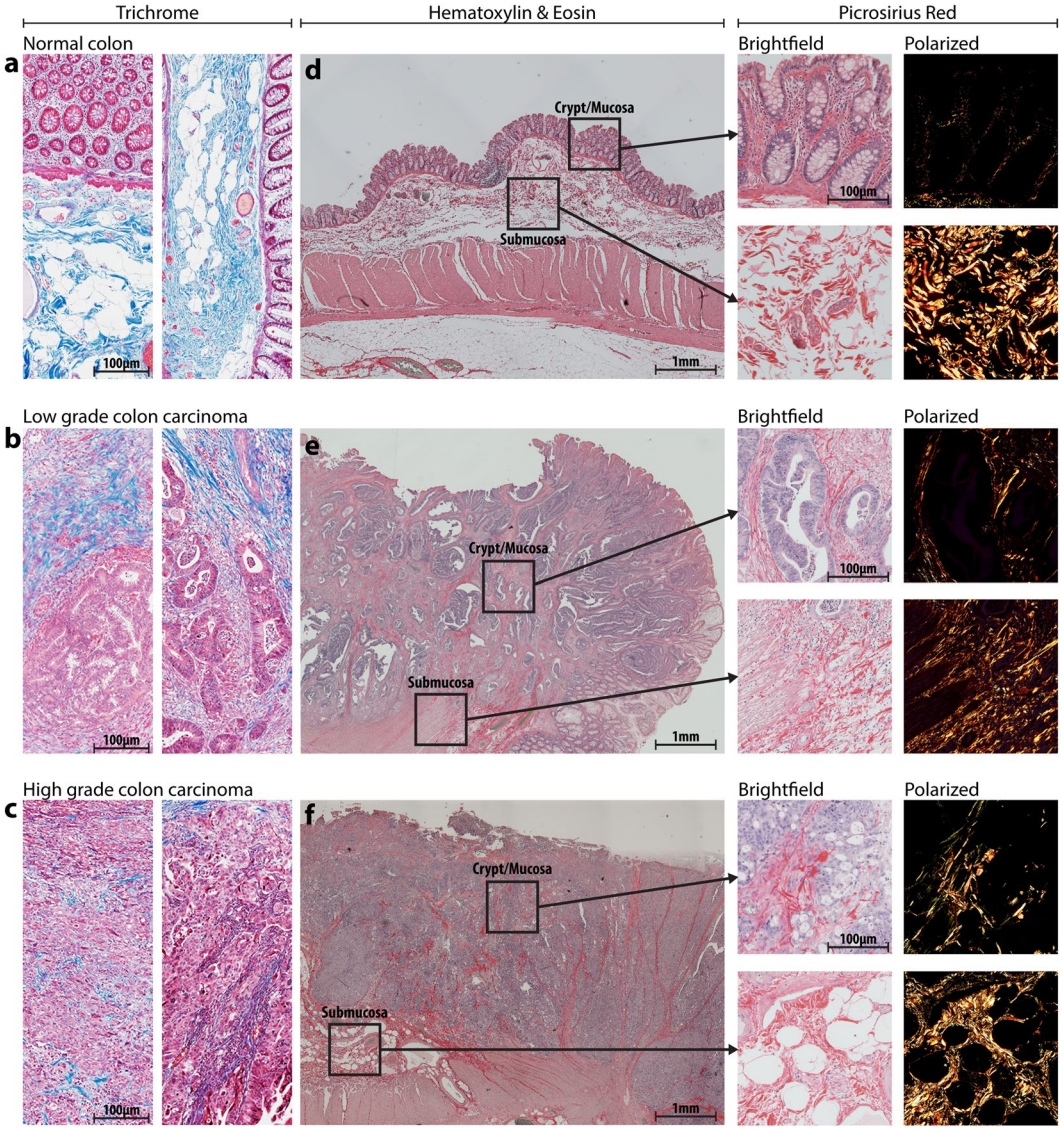

Figure 1. Clinical colorectal cancer sample morphology, collagen structure, and compartments. Clinical samples of varied grade, as indicated, were obtained initially stained with Masson's Trichrome (**a–c**) to visualize collagen (blue signal) structure, density, and localization. H&E staining and imaging was used to qualitatively separate the tissue into mucosal and submucosal compartments (**d–f**). Then, PRS staining was performed and imaged to isolate collagen fibers specifically.

we characterized collagen fiber bundling and micro-architecture in samples cultured *in vitro* and in samples implanted in mice. An additional goal was to determine if co-cultures formed *in vitro* could retain collagen fiber organization under physiological conditions *in vivo*. Similar to the analysis of collagen fiber organization in the clinical specimens (Fig. 2), we used PSR staining and image segmentation tools to assess collagen fiber features in the *in vitro* cultured and *in vivo* explanted samples (Fig. 3)[29]. Visual inspection of the stained collagen fibers showed that the LX2 co-cultures produce increased red and orange signal *in vitro* and *in vivo* compared with the collagen-only constructs (Fig. 3a). Hue analysis corroborated these findings and showed that LX2 co-cultures grown for 7 days *in vitro* produced bundled collagen fibers with higher levels of orange and yellow collagen (Fig. 3b) suggesting that these samples were more organized compared with collagen-only samples. Similarly, samples explanted after 14 days showed that LX2 co-cultures possessed higher degrees of bundling with significantly higher amounts of red and orange signal compared with collagen-only constructs.

Quantitative analysis of collagen fiber organization showed a wider angular distribution in LX2 co-cultures compared with collagen-only conditions (Fig. 3c). However, in *in vivo* explanted samples no significant difference was observed in the angular distributions of collagen fibers between groups, suggesting a similar, random, assortment of fibers overall (Fig. 3c). On the other hand, fiber length and width were significantly higher in the LX2 co-cultures *in vitro* compared with collagen-only constructs and this trend was similar for *in vivo* explanted samples (Fig. 3d,e). Together, these results suggest that LX2 remodeling of collagen *in vitro* generates more bundled and ordered fiber micro-structures and importantly, these ordered collagen fiber features were

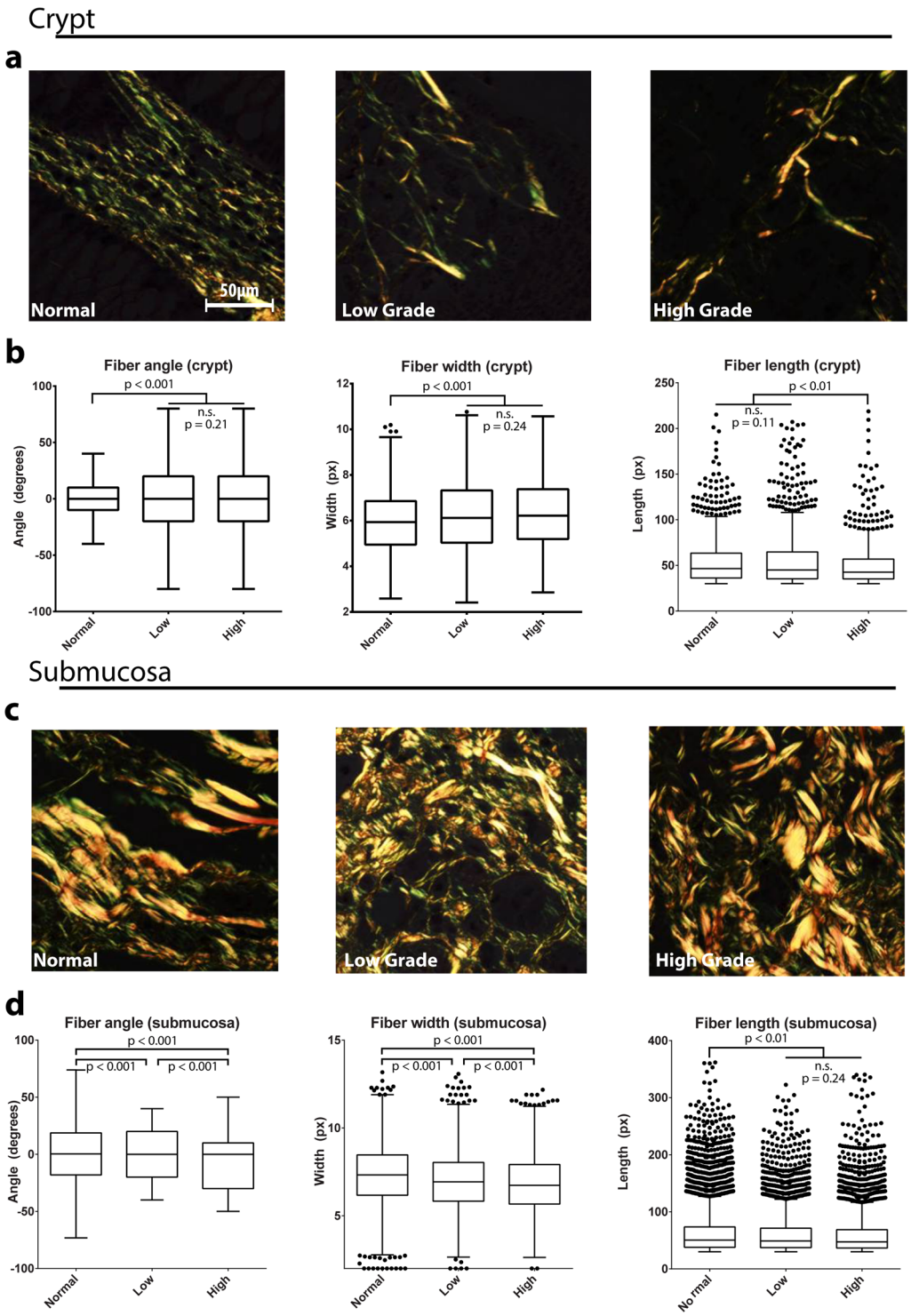

Figure 2. Microarchitecture of clinical samples. Regions of interest (ROIs) from the crypt and submucosal compartments of clinical samples of varying grade ($n > 10$ ROIs from $n = 4$ individual samples for each condition), as indicated, were PRS stained and imaged under polarized light (**a,c**). Fiber architecture was analyzed with segmentation software (CT-FIRE) to generate distributions of fiber angle, width, and length (**b,d**). Graphs of fiber hue represent mean + s.e.m. of experiments performed in triplicate (three imaging fields from each patient). Graphs of fiber angle, length, and width are box and whisker plots with Tukey formatting of pooled fibers from four regions of interest from each patient, representing 500–4000 fibers in total; individually drawn points lie beyond 1.5 * inter-quartile range of the plot.

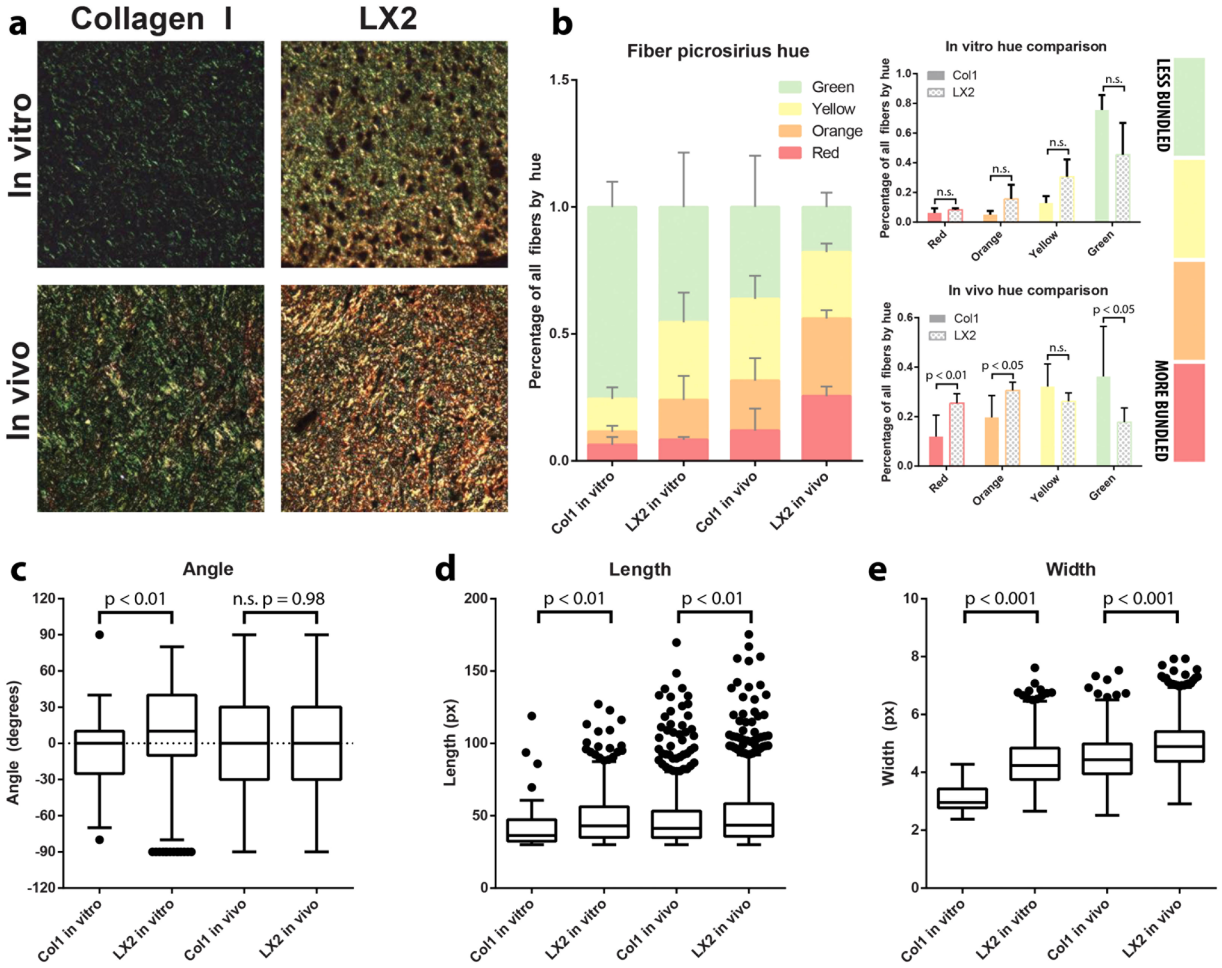

Figure 3. Construct extracellular matrix (ECM) organization *in vitro* and *in vivo*. Collagen fiber microarchitecture in collagen-only constructs and LX2 co-cultures, *in vitro* and *in vivo*, as indicated, was visualized with PRS (**a**). Fiber bundling was quantified through signal hue analysis (**b**): green and yellow signal indicate less bundled fibers and orange and red signal indicate more bundling. Collagen fibers were quantified with segmentation software (CT-FIRE). Distributions of angle (**c**), length (**d**), and width (**e**) of fibers were obtained from samples *in vitro* and *in vivo*. Graphs of fiber hue represent mean + s.e.m. of experiments performed in triplicate. Graphs of fiber angle, length, and width are box and whisker plots with Tukey formatting of pooled fibers from experiments performed in quadruplicate or greater; individually drawn points lie beyond 1.5 * inter-quartile range of the plot.

maintained after 14 days of *in vivo* implantation. Furthermore, the differences in collagen fiber organization between LX2-containing co-cultures and collagen-only constructs simulate differences between healthy colon and low-, or high-grade CRC, respectively.

Tumor spheroids grow slower in structurally organized microenvironments. Next, we tested the effects of the microenvironmental (collagen fiber) organization on tumor cells present within samples with distinct collagen fiber features. We inserted spheroids of HCT116, a metastatic CRC cell line, into both LX2-contaning co-cultures and collagen-only constructs (Suppl. Figure 1b) and analyzed tumor cell phenotype in *in vitro* cultured and *in vivo* implanted samples.

H&E-stained images show that HCT116 spheroids inside the LX2 organized matrix remained compact and were significantly smaller than those within collagen-only matrices after 7 days (Fig. 4ai-**lower, c**), and continued to decrease in size and retained a compact, epithelial-like morphology by 28 days. In contrast, HCT116 cells embedded in collagen-only constructs migrated outside the initial spheroid body, and after 7 days, protrusions of cells were apparent in most radial directions. This migratory behavior continued and resulted in a significant increase in aggregate size after 28 days (Fig. 4ai-**upper, c**), and loss of compact morphology, possibly due to a mesenchymal phenotype induced by the unstructured matrix organization, as we have previously shown[16]. Progressive measurements of HCT116 spheroid growth over time indicated that spheroids in LX2 co-cultures were size restricted, and even exhibited size reduction, whereas HCT116 spheroids in collagen-only constructs were able to expand (Fig. 4c). Although the HCT116 do not recreate the glandular structure of physiologic colon mucosa, the overall differences in cellular morphology between groups indicates phenotypic changes induced by microenvironmental alterations.

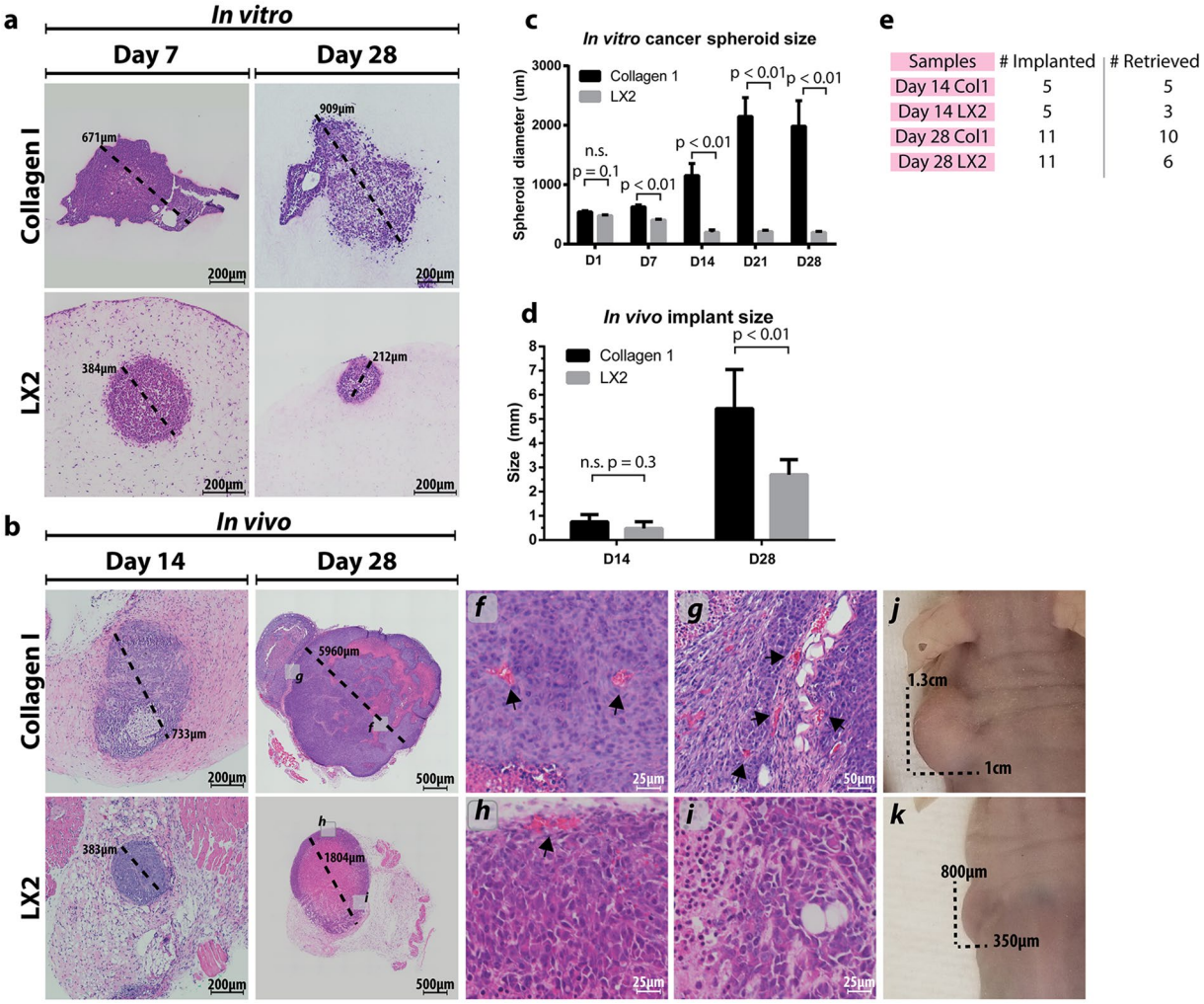

e

Samples	# Implanted	# Retrieved
Day 14 Col1	5	5
Day 14 LX2	5	3
Day 28 Col1	11	10
Day 28 LX2	11	6

Figure 4. Tumor construct morphology and growth *in vitro* and *in vivo*. Tumor spheroid morphology was visualized on days 7 and 28 *in vitro* (**a**) and *in vivo* (**b**) in both collagen-only constructs and LX2 co-cultures, as indicated. Integration of vasculature was also observed at day 28 of *in vivo* implanted samples (insets **f–i**). Spheroid diameter was tracked over time *in vitro* (**c**), and *in vivo* implanted samples were measured at the time of explantation for average diameter (**d**). Examples of gross implant size *in vivo* can be seen in insets **j**, **k**. Implant retrieval data for the *in vivo* studies (**e**). Graphs represent mean + s.e.m. of experiments performed in triplicate.

Next, we analyzed the size and morphology of *in vivo* implanted LX2 co-cultures and collagen-only samples after 14 and 28 days (Fig. 4b). H&E-stained images indicate that HCT116 spheroid growth in LX2 co-cultures was restricted at day 14, and a large necrotic core had formed by day 28, although the tumor compartment had continued to grow in size. Blood vessels were evident at the perimeters of the tumor compartment in the LX2 co-cultures, suggesting that the tumor cells failed to induce neovascularization inside the tumor mass (Fig. 4b **inset h & i**). Conversely, HCT116 spheroids in collagen-only constructs grew rapidly and by day 28, the majority of the HCT116 tumor compartment appeared viable with a low proportion of necrotic area and extensive neovascularization in the tumor mass (Fig. 4b-**upper and inset f & g**). Overall, collagen-only explants contained an average of 35 vessels compared to approximately 4 in explanted LX2 co-cultures (Suppl. Fig. 2). Size measurements of explants showed no differences in average implant diameter explanted at day 14, however LX2 co-cultures were significantly smaller compared to collagen-only constructs by day 28 (Fig. 4d) and significant size differences could be observed before excision (Fig. 4b **inset j & k**). Of note the number of samples that could be explanted were different between the two groups. Fewer LX2 co-cultures were successfully retrieved compared with collagen-only constructs at both day 14 (LX2: 60%; Col: 100%) and day 28 (LX2: 55%; Col: 91%) (Fig. 4e), suggesting that the presence of LX2 cells in the samples represses the growth of the HCT116 spheroids and could lead to the loss of the tumor construct tissue.

Relationships between collagen fiber organization and architecture and cancer cell phenotype in 3D CRC constructs and CRC tissue biopsies. Tumor spheroid growth in constructs of different collagen architectures suggested that it may simulate differences between low and high-grade cancers. We previously

observed that collagen fiber micro-architecture and topography had a significant impact on EMT in CRC cells in these 3D samples[16]. Accordingly, to assess phenotypic similarities between co-cultured constructs and biopsied tissue, we performed immunohistochemistry (IHC) analysis on tissue sections from 3D CRC constructs and CRC tissue biopsies for markers associated with EMT and oncogenesis (Suppl. Fig. 3–7) and used custom segmentation algorithms in Visiopharm to quantify their expression.

Tumor cell proliferation was determined by staining for Ki-67 and analyzing its nuclear expression (Suppl. Fig. 3). In both *in vitro* cultured and *in vivo* explanted samples, Ki-67 expression was higher in collagen-only constructs compared with LX2 co-cultures. (Fig. 5a). E-Cadherin is a cell-cell adhesion protein, present in healthy colonic epithelial cells and can be lost when cancer cells undergo EMT[33–35]. E-Cadherin was found around the cell membrane and appeared continuous around positive cells in IHC images (Suppl. Fig. 4). We quantified E-Cadherin expression by counting cells with completely stained membranes only (Fig. 5b). *In vitro*, LX2 co-cultures showed significantly higher expression of E-Cadherin compared with collagen-only constructs. *In vivo*, no significant differences in E-Cadherin expression were observed between groups (Fig. 5b). N-Cadherin is another cell-cell adhesion protein that is typically found in colorectal cancer cells that have undergone EMT[36]. We quantified N-Cadherin in the same manner as E-Cadherin, but also counted cells with nuclear expression of N-Cadherin as that is indicative of cytoplasmic expression that has not fully localized to the membrane (Suppl. Fig. 5)[36]. Collagen-only constructs displayed significantly higher levels of N-Cadherin expression compared to LX2 co-cultures both *in vitro* and *in vivo* (Suppl. Fig. 4 and 5c). The WNT/β-Catenin pathway is an important pathway associated with EMT, in which β-Catenin protein ultimately accumulates in the nucleus where it acts as part of a transcription factor complex and facilitates the upregulation of a host of oncogenic processes[37]. We quantified β-Catenin expression by counting cells with positive nuclear-localized β-Catenin signal (Suppl. Fig. 6). Collagen-only constructs had higher levels of nuclear β-Catenin compared with LX2 co-cultures in both *in vitro* and *in vivo* groups, although the difference was not statistically significant (*in vitro:* $p = 0.058$) (Fig. 5d). The focal adhesion kinase (FAK) pathway is also associated with oncogenesis and EMT. FAK is a tyrosine-kinase that forms adhesions with matrix components, and high levels of FAK are found in aggressive cancer cells, whereas knockdown of FAK can reduce or eliminate cancer cell motility[38]. We quantified FAK by measuring the positively stained area fraction of the total tumor area (Suppl. Fig. 7). FAK expression was significantly higher in collagen-only samples compared with LX2 co-cultures in both *in vitro* and *in vivo* groups (Fig. 5e). This result suggests that in collagen-only constructs cancer cell motility could be enhanced. Together, analysis of this selected protein expression panel indicates that tumor cell spheroids embedded in collagen-only constructs demonstrated a mesenchymal phenotype with de-differentiated features, compared to cancer cells embedded in LX2 containing co-cultures which appeared more phenotypically epithelial. In addition, this dataset indicates *in vivo* implantation of our 3D model retains ECM driven phenotypes

Next, we performed the same IHC analysis on clinical biopsies to assess whether our fabricated samples were capturing clinically relevant phenotypes. We utilized healthy tissue alongside low- and high-grade CRC biopsies. Increasing Ki-67 expression was associated with higher grading in tumor samples (Fig. 5a). CRC tumor biopsies demonstrated a significant decrease in E-Cadherin expression, compared with healthy colonic tissue and the expression further decreased with increasing tumor grade (Fig. 5b). CRC tumor biopsies and healthy colonic tissue showed very low N-Cadherin expression overall with about 1–3% of cancer cells positive for N-Cadherin staining (Fig. 5c). Tumor tissue specimen derived from patients with high-grade CRC exhibited the highest levels of nuclear β-Catenin expression, corroborating the previous results that higher grades of CRC are associated with EMT (Fig. 5d). Interestingly, low-grade tumor specimen demonstrated the highest FAK expression while high-grade tumor specimen had increased expression compared to normal colonic tissue, but a lower expression compared to low-grade (Fig. 5e).

Tumor spheroids grown in unorganized microenvironments are more sensitive to chemotherapeutics. Since the HCT116 tumor spheroids demonstrated significantly different phenotypes in LX2 co-cultures and collagen-only samples, we speculated that they will also have different responses to clinically used chemotherapeutic agents. To test this hypothesis, we exposed tumor spheroid bearing samples to 4 drugs: 5-Fluorouracil (5-FU), which disrupts thymidylate synthase[39], and its clinically-used drug combinations FOLFOX and FOLFIRI, and a targeted therapy, Regorafenib. FOLFOX is a 5-FU combination with folic acid (leucovorin) and oxaliplatin (platinum-based antineoplastic)[40]. FOLFIRI is a combination of 5-FU, folic acid, and irinotecan (topoisomerase inhibitor)[40]. Regorafenib is a multi-receptor tyrosine kinase inhibitor[41].

Cultures were treated for 72 hours, then harvested and stained for Ki67 and Caspase 3 in order to determine the proportion of cells that were either actively proliferating, apoptotic, or neither (Fig. 6a,b). All chemotherapeutics had minimal effect on apoptosis of tumor cells within an LX2-organized stroma. In contrast, HCT116 spheroids in collagen-only constructs were highly sensitive to all 5-FU and its combinations and displayed significantly higher levels of apoptotic cells compared to LX2 co-cultures. On the other hand, all chemotherapeutics arrested the proliferation of the tumor cells in both LX2 co-cultures and collagen-only constructs. However, the effects of 5-FU and FOLFOX on tumor cell growth arrest was significantly higher in collagen-only constructs compared with LX2 co-cultures. Interestingly, the effects of FOLFIRI treatment on growth arrest was significantly higher in LX2 co-cultures compared with collagen-only constructs. Finally, Regorafenib induced a significant growth arrest in tumor cells, but with little difference between LX2 co-cultures and collagen-only constructs.

Cancer stem cells are often considered as less chemotherapy-responsive compared with the rest of the tumor cell population. HCT116 and other CRC cells were reported to express several known CSC markers, especially CD44 and CD133[42]. To identify potential differences in stem cell markers between samples with ordered (LX2) and disordered (collagen-only) stromas, we measured CD44 and CD133 expression in HCT116 spheroids in these environments using Visiopharm quantified IHC (Fig. 6d). CD44 was expressed in both LX2 co-cultures and collagen-only constructs with significantly higher levels found in collagen-only vs. LX2 samples (Fig. 6c). CD133

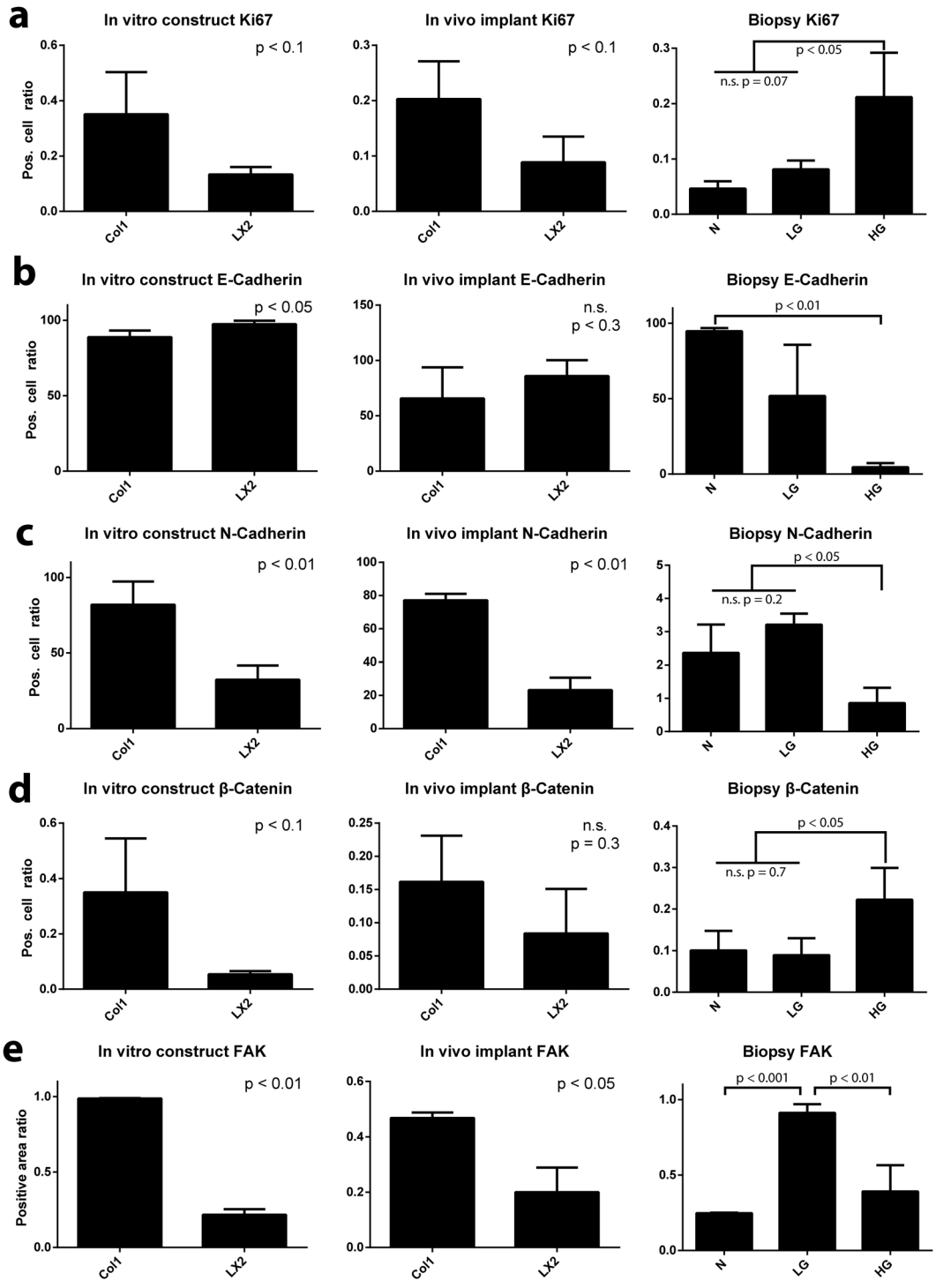

Figure 5. Immunophenotyping of tumor cells within fabricated constructs and clinical sample. Samples from constructs cultured *in vitro*, constructs implanted *in vivo*, and clinical CRC biopsies of varying grade were immune-stained for markers related to EMT and oncogenesis, as indicated. Staining results were analyzed using Visiopharm and graphed as the proportion of cancer cells with: (**a**) nuclear localization of Ki67; (**b**) with fully intact, membrane localized E-Cadherin expression; (**c**) with N-Cadherin expression; (**d**) with nuclear localization of β-Catenin. (**e**) Ratio of total area corresponding to positive FAK expression in tumor spheroid and clinical CRC biopsies of varying grade. Graphs represent mean + s.e.m. of three regions of interest from each sample of experiments performed in triplicate.

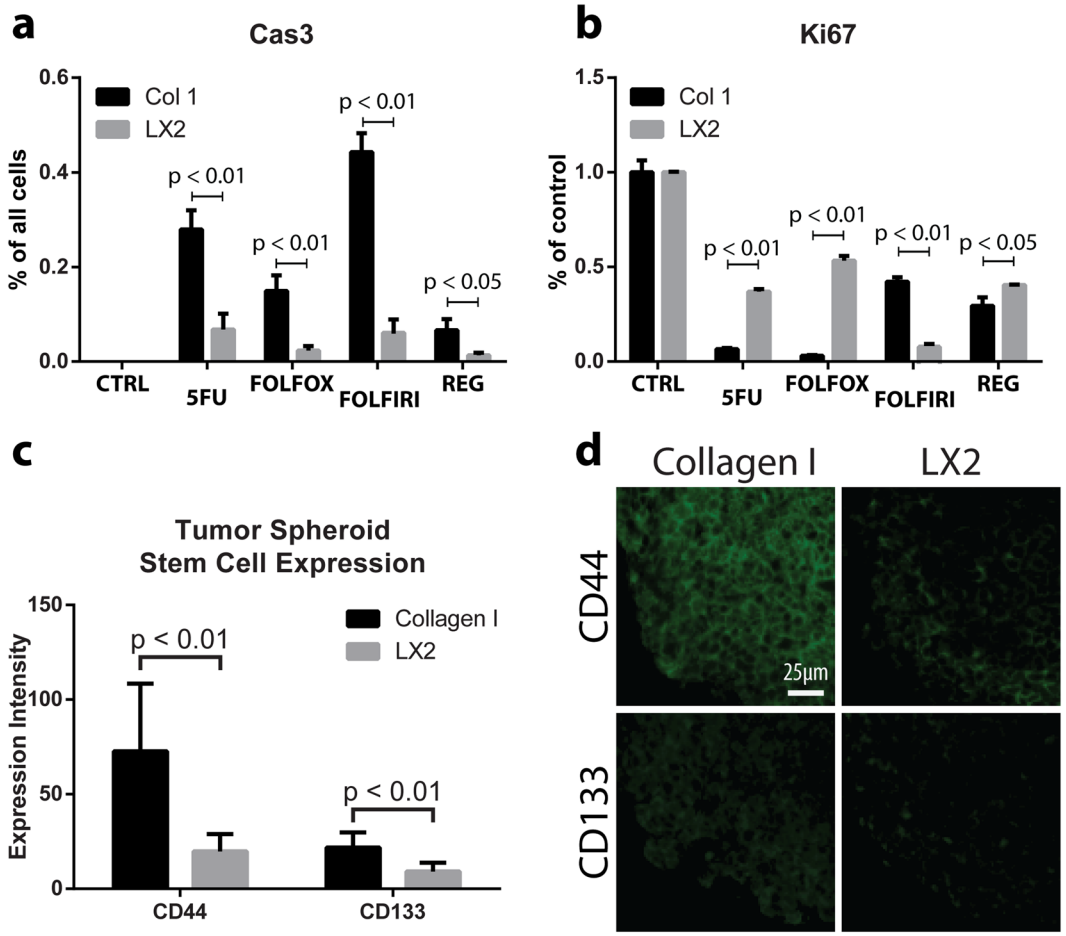

Figure 6. Chemotherapeutic sensitivity and expression of cancer stem cell markers in CRC constructs. Collagen-only constructs and LX2 co-cultures, as indicated, were exposed to various chemotherapeutics for 72 hours, and the expression of Caspase3 (measured as percent of all cells) (**a**) and Ki67 (measured as percent of control) was analyzed (**b**). CD44 and CD133 expression was quantified in collagen-only construct and LX2 co-culture samples, as indicated, (**c**) using IHC (**d**). Graphs represent mean + s.e.m. of three regions of interest from each sample of experiments performed in triplicate or greater.

expression was lower, by comparison to CD44 expression, but similarly, was higher in collagen-only constructs compared to LX2 co-cultures. These results suggest that disordered, collagen-based stroma, enriches the cancer stem cell population in HCT116 spheroids embedded in collagen-only environments.

Discussion

In patients, tumors grow and progress over many years, often-times remaining in a non-invasive equilibrium for extended periods without producing any outward symptoms. Events, not fully understood, shift the tumor from a non-invasive phenotype towards an invasive one that is associated with rapid changes to the TME, including ECM degradation and stromal cell activation, and tumor cell migration and proliferation. Although 2D cell culture has led to many breakthroughs in cancer research, it cannot replicate the nuances of the TME which have been found to significantly affect tumor progression. Not only are tumors composed of a myriad of cell types that secrete a unique combination of signaling factors, but cancerous cells are attached to, and often-times require, the latticework of proteins that comprise the ECM – the physical TME. This means that therapeutics developed in 2D culture systems may not translate well to treating tumors *in vivo*, impacting patients as well as leading to high drug development costs. 3D tumor modeling technology, developed in recent years, addresses the deficiencies of traditional cell culture systems by replicating some of the unique features of the TME[16–18]. We have recently published several studies describing bioengineered tumor technology, which allows systematic manipulation of structural features of the TME and subsequent testing of the effects on tumor cell phenotype[16–18]. Despite the value of 3D tumor models, their maintenance under artificial culture conditions *in vitro* cannot fully assess tumor progression *in vivo*. On the other hand, *in vivo* mouse models are poor mimics of human physiology and tumor growth kinetics, as the TME will be largely composed of murine components. One of the goals of this study was to transition the replicative features of *in vitro* bioengineered models into an *in vivo* model to capture the best of both methods. We replicated native TME architecture, as observed in clinical biopsies, with 3D CRC constructs, then implanted them into nude mice to expose them to *in vivo* physiology. Our results demonstrate that bioengineered constructs, fabricated to recapitulate the TME of different tumor grades maintained ECM architectural

features for up to 4 weeks *in vivo*, and furthermore, CRC cells retained their phenotype after *in vivo* implantation. Although HCT116 cells may not fully capture many of the nuances of clinical tumor cases due to their long-term culture under *in vitro* conditions; the phenotypic similarities between *in vitro*/*in vivo* HCT116 constructs and clinical samples show promising correlation.

In the current study we used hepatic stellate cells (LX2) to simulate stromal cells that are involved in collagen remodeling of the liver metastasis microenvironment[8,43–45]. The results, demonstrating that LX2-mediated ECM structured microarchitecture pushes the HCT116 metastatic CRC cells towards an epithelial phenotype vs. a mesenchymal phenotype induced by unstructured ECM architecture are especially intriguing as they suggest that under certain conditions the hepatic stellate cells, commonly known to support EMT and growth of liver metastasis[16,32,46], may act to suppress growth and spreading of metastasis if given an opportunity to create structured matrix around the metastatic foci. Furthermore, HCT116 cells demonstrated reduced chemotherapeutic sensitivity in the LX2 co-cultures as well. Others have also targeted hepatic stellate cells (HSCs) as possible TAFs and as contributors to fostering a premetastatic environment for CRC cells. For example, addition of conditioned media from activated-HSCs to CRC cells in 2D culture resulted in increased motility and invasive characteristics of the tumor cells[32]. This data suggests a paracrine effect of HSCs on the tumor cells however, these studies were performed in a non-physiologic 2D culture system, which does not capture important features of the TME, like our 3D model can. Although paracrine secretion of factors from TAFs can clearly drive cancer progression, TAF's involvement does not stop at the level of external cell signaling; in fact, we previously measured the effect of paracrine signaling from stromal cells on growth, phenotype, and chemotherapeutic response of HCT116 cells in a similar culture format described here, and found nominal effects compared to those imparted by collagen remodeling[47]. TAFs have the ability to change ECM structure and organization, and understanding the subsequent effects on cancer cells is an important step towards more accurately modeling the TAF-cancer cell axis.

A major motivation of this research is to create a better *in vitro* model of tumor tissue by including, alongside the tumor cells, stromal cells and ECM. To achieve this aim, we utilized a bottom-up approach to replicate the distinct compartments of tumor tissue, as observed in Fig. 1. The native colonic submucosa is collagen-rich and populated by a mixture of SMCs, fibroblasts, adipose and immune cells which informed our decision to utilize collagen as the base hydrogel with fibroblasts as the main stromal component. However, the exclusion of immune cells represents a weakness in our model, especially as the immune component's role in the TME is actively studied and targeted in contemporary research and therapeutic development. In addition, tumor compartments in biopsies were typified by aggregates (foci) of cancer cells which we simulated with a cancer spheroid. This approach replicated the dense cellularity, diffusion kinetics, and cell-cell contacts evident in human tumors, however, it fails to capture the glandular morphologies found in well-differentiated CRC cases. Our system is inherently modular as well; each compartment can be modified independently to replicate the tumor-stroma dynamics of a wide variety of tumor etiologies. The HCT-116 cells used here can be replaced by cells of lower malignancy, patient cells, or a heterogenous mixture of cancer cells. Importantly, although HCT116 cells have a strong record of modeling CRC *in vitro*, future studies will benefit tremendously from the inclusion of patient derived CRC cells. The stromal compartment can be modified to include a wider range of cells, higher concentrations of collagen, or different ECM components such as laminin, fibronectin, or elastin. In our previous work, we utilized colonic smooth muscle cells within the stromal compartment to replicate the native, healthy colon[16]. We also previously demonstrated that stromal cells in our platform are responsive to biochemical manipulation, in this case to aminopropionitrile (BAPN), an inhibitor of lysyl oxidase, which decreased smooth muscle cell collagen remodeling capability. In human tumors, a panoply of paracrine signals (TGFβ1, PDGF, IL-1β, etc.) drive stromal cell involvement, many of which can be modeled within our system. In fact, exposure of tumor constructs to TGFβ1 further stimulated ECM restructuring, creating highly bundled collagen fibers and resulting in stiffer matrices (manuscript in preparation). Physiologically, the balance between stromal cell-mediated construction and tumor cell-mediated degradation of ECM contributes to tumor cell migration although this dynamic is not fully understood.

An important observation of this study is the consistency of results between the *in vitro* experiments and under physiological conditions *in vivo*, both of which agree with our prior findings[16,18]. Immunophenotyping results (Fig. 5) indicate the specific architecture of the niche may help determine EMT or MET phenotype of liver metastatic tumor cells, and could explain why some tumors do not respond well to non-combinatory, anti-proliferative chemotherapies[9]. Further, we can challenge our model with a large library of small molecule inhibitors, chemotherapeutics (Fig. 6a,b), and experimental compounds. Interestingly, we observed an increase in stem cell marker expression in tumor cells within collagen only environments, which may point towards ECM-driven cancer stem cell enrichment. Future directions may include assessment of patient-derived tumor cell phenotype and drug response then using mathematical modeling to transfer results found *in vitro* to predictive information for patient prognosis or drug efficacy. Lastly, we have demonstrated that fiber organization and fibroblast-mediated ECM remodeling appears to affect cancer cells and is correlated with cancer grades in clinical specimens, indicating these metrics have significant potential to be used as prognostic and/or diagnostic tools.

Overall, this study is the first to characterize an *in vitro* model of the TME based on observations of native tissue and validate it in the context of whole-body physiology. Non-traditional treatment vectors that target the ECM or stromal cells might provide valuable avenues for developing novel treatments or co-therapies that synergize with existing chemotherapeutic or radiation technologies. By controlling cancer cell responsiveness through changes to the TME, lower doses of chemotherapy or radiation could become effective thereby reducing or eliminating many of the undesirable side-effects of traditional cancer therapies (*e.g.*, cytotoxicity in healthy tissues), as well as yielding lower tumor cell resistance rates. 3D bioengineered constructs are a promising modality for drug development and screening because they can reproduce human physiology at a high level. However, understanding of pharmacokinetics and pharmacodynamics still necessitates the use of animal models that are, however, not without their own limitations when being translated to humans. Here, we bridge the gap between *in vitro* study

and animal modeling by utilizing implanted human tumor constructs, and outline a novel mechanism of cancer cell control – ECM microarchitecture.

Materials and Methods

Cell culture. Human hepatic stellate cells, LX2 cells, were provided by Dr. Scott Friedman (Icahn School of Medicine at Mount Sinai, New York, NY). Human colorectal carcinoma cells, HCT116 cells, were obtained from ATCC (#CCL-247, ATCC, Manassas, VA). Both cell types were cultured and expanded in tissue culture-treated plastic dishes. Cultures were passaged when cells reached 70–90% confluency. Both cell types were cultured with Dulbecco's Minimum Essential Medium (DMEM, Millipore-Sigma, St. Louis, MO) containing 10% fetal bovine serum (FBS, Hyclone, Logan, UT). Cells were detached from the substrate with Trypsin/EDTA (Hyclone) and resuspended in media before use in construct or spheroid fabrication. Use of LX2 cultures was discontinued after the ninth passage and a fresh vial was continued instead.

Construct fabrication. Spheroids of HCT116 cells (1.0×10^4 cells each) were prepared by homogenously suspending cells in culture media at 1.0×10^5 cells/mL followed by dispensing 100 µL of cell-media suspension into each well of an ultra-low attachment round-bottom 96-well plate (CoStar #7007, Corning, Corning, NY). Cells were observed each day for 3 days, by then spheroids had formed tight clusters without irregularity, and used immediately for construct fabrication.

3D constructs were fabricated as described recently (Suppl. Fig. 1a)[16]. Type I Rat Tail Collagen (#354236, Corning) was prepared according to the manufacturer's protocol at a concentration of 2 mg/mL. LX2 cells were trypsinized and counted, then suspended in prepared collagen at 5.0×10^6 cells/mL. Media from plates containing spheroids was aspirated, and 100 µL of LX2-collagen solution was pipetted into each spheroid well, carefully to avoid disturbing the spheroid structure. The LX2-collagen-spheroid mixture was slowly pipetted up and down to suspend the spheroid, then the whole volume was dispensed into a custom polydimethylsiloxane (DOW Sylgard 184, Midland, MI) mold [16] ensuring relatively central placement of the spheroid within the polymerizing hydrogel (30 min at 37 °C) (Suppl. Fig. 1a). Upon complete collagen polymerization, media was slowly added and molds were removed. Samples were cultured for varying durations depending on the scope of the experiment.

Subcutaneous implantation. Six-week-old female athymic nude mice were obtained from Charles River Laboratories (Wilmington, MA). Animals were anesthetized using 2% isoflurane and given a pre-operative subcutaneous injection of 5 mg/kg ketoprofen. Two small skin incisions were made on the dorsal side approximately 15 mm from the midline. Subcutaneous pockets were generated using blunt dissection and implanted with one sample per site. Incisions were closed with 4–0 vicryl suture (Ethicon, Somerville, NJ) and dressed with Tegaderm film (3 M, Maplewood, MN). All procedures were performed in strict accordance with the NIH Guide for the Care and Use of Laboratory Animals, and the policies of the Wake Forest University Institutional Animal Care and Use Committee (IACUC). The study was approved by the Wake Forest University IACUC, Protocol No. A17–036. Animals were euthanized at 2 and 4 weeks by CO_2 asphyxiation followed by cervical dislocation. Skin flaps were opened and explants retrieved.

Gross morphological assessment. Gross macroscopic images of *in vivo* explants were taken with a smartphone camera (Samsung, Seoul, South Korea) with a metric ruler held within the frame of the image. ImageJ software (National Institutes of Health, Bethesda, MD) was used to assess explant size after initial calibration.

Chemotherapy treatments. Constructs with embedded spheroids were cultured for 72 hours, then transferred to new well plates and incubated with media containing chemotherapeutics. Samples were exposed to chemotherapeutics for a further 72 hours before analysis. Chemotherapeutic formulations were prepared using the following concentrations: 5-Fluorouracil 1 mM, Oxaliplatin 25 µM, Irinotecan 50 µM, Leucovorin 50 µM, and Regorafenib 50 µM.

Human samples. Slides from de-identified CRC patients were purchased from the Wake Forest Tumor Tissue and Shared Pathology Resource core. Samples were selected randomly from the patient pool with a specified tumor grade (well- or poorly differentiated) and corresponding non-tumor containing (healthy tissue) slides were obtained for each patient. All clinical grading and pathology analyses were performed by a board-certified pathologist. Human samples were formalin fixed prior to histological processing.

Histological and immunohistochemical (IHC) analysis. *In vitro* and animal samples were fixed in 4% paraformaldehyde overnight at 4 °C, then washed with phosphate buffered saline (PBS), and stored in 70% ethanol. Following paraffin processing and embedding, 5 µm serial sections were cut using a microtome (Leica Microsystems Inc., Buffalo Grove, IL) and mounted to slides. For all staining procedures, slides were baked for 1 h at 60 °C followed by standard deparaffinization and rehydration. Hematoxylin & Eosin (H&E) staining was performed by core facilities at the Wake Forest Institute for Regenerative Medicine. Picrosirius Red (PRS) staining was done using a commercial staining kit (#24901, PolySciences, Warrington, PA) following the manufacturer's protocol. Masson's Trichrome staining was performed using a commercial staining kit (#HT15, Millipore-Sigma) following the manufacturer's protocol.

For immunohistochemistry (IHC), all incubations were performed at room temperature unless otherwise stated. Antigen retrieval was performed using Proteinase K (DAKO, Carpinteria, CA) incubation for 15 min. Samples were permeabilized with 0.05% Triton-X (Millipore-Sigma) in PBS for 5 min. Non-specific antigen blocking was performed using Protein Block Solution (#ab156024, Abcam, Cambridge, MA) incubation for 30 min. Slides were then incubated with the appropriate primary antibody against CK-18 (#ab82254, Abcam), FAK (#ab40794, Abcam), β-Catenin (#71-2700, Invitrogen-ThermoFisher), E-Cadherin (#ab40772, Abcam),

N-Cadherin (#ab76011, Abcam), CD44 (#ab51037, Abcam), CD133 (#orb10288, biorbyt, San Francisco, CA) or Ki-67 (#ab16667, Abcam) at recommended dilutions in a humidified chamber overnight at 4 °C. Next, slides were thoroughly washed and incubated for 1 h with the appropriate secondary antibody: biotinylated anti-rabbit (BA-1000, Vector Laboratories) or biotinylated anti-mouse (BA-2000, Vector Laboratories) for chromogenic samples; anti-rabbit Alexa Fluor 647 secondary (#ab150075, Abcam) or anti-mouse Alexa Fluor 594 antibodies (#ab150116, Abcam) (1:200 dilution) for fluorescent samples. Cells were counterstained with DAPI for 5 minutes, and washed 3 times with 1X PBS prior to fluorescent imaging. Due to the formalin fixation of human samples, significant autofluorescence is produced necessitating chromogenic labeling. All samples compared directly to human samples were also chromogenically processed for consistency of comparison. For chromogenic processed samples, slides were then washed and incubated with VECTASTAIN ABC reagent (PK-4000, Vector Laboratories) for 30 min. Signal exposure was timed and visualized while slides were incubated with DAB (SK-4105, Vector Laboratories) or Vector Red (SK-5105, Vector Laboratories) substrate. Double-stained slides followed this protocol twice in succession for each individual marker. Vector Red substrate was used first and DAB second. Relevant control slides were prepared for each condition and each antibody combination by omitting the primary antibody incubation. Slides were mounted with MM24 (#3801120, Leica, Wetzlar, Germany), and light microscopy images, using linearly polarized light for PSR-stained sections, were captured with an Olympus BX63 microscope (Olympus, Center Valley, PA) with an Olympus DP80 camera (Olympus).

Image analysis and quantification. Spheroid size was assessed using H&E-stained light micrographs and a MatLab (2018b, MathWorks, Natick, MA) script to quantify average diameter. Counts of infiltrative blood vessels and vessel size were quantified using a Matlab script. Images were captured with an Olympus IX83 microscope (Olympus, Center Valley, PA) equipped with a Hamamatsu Orca-Flash 4.0 camera (Hamamatsu, Shizuoka, Japan).

PRS signal was quantified in two ways: hue analysis of collagen signal and collagen fiber geometric parameter segmentation. Hue analysis to identify different levels of collagen bundling and fibrilization was performed using a Matlab script. Fiber parameter segmentation and quantification was performed using CT-FIRE (Laboratory for Optical and Computation Instrumentation, University of Wisconsin)[29].

Masson's Trichrome signal hue was quantified similarly to PRS hue analysis. Red and blue pixels were identified and counted using a Matlab script. Ratios of colored pixels versus total tissue pixels were then calculated for comparison.

IHC images were imported as uncompressed files into Visiopharm software (Broomfield, CO) for analysis and quantification. In samples where tumor cells were difficult to distinguish from stromal cells (*in vitro* and *in vivo* implanted constructs), a script was written to deconvolve Vector Red signal, then isolate Vector Red stained CK-18 positive cells which specifically labels HCT116 cells. After HCT116 cells were segmented, a second script was written to deconvolve DAB signal and quantify the expression or localization of: β-catenin, E-Cadherin, FAK, Ki67, and N-Cadherin (Suppl. Fig. 13). For β-catenin and Ki67, nuclei were marked as positive or negative for DAB staining and counted. For E-Cadherin and N-Cadherin, cells were marked positive if they had complete membrane localization of DAB and negative if not. For FAK, ratios of total tumor area that stained positive for DAB were generated.

For analysis of stem cell markers CD44 and CD133, a script was written to mark cells with complete membrane localization of signal as positive and negative if not. For analysis of Caspase 3 staining in drug treated samples, a script was written to identify membrane and cytoplasmic localization of signal; cells were marked positive if they had positive Caspase 3 signal. For analysis of Ki67 staining in drug treated samples, a script was written to segment nuclear Ki67 signal and marked cells positive if they had nuclear colocalization of Ki67 signal.

Statistical analysis. All experiments were performed using $n = 3$ unless otherwise stated. Statistical analysis of parametric data was performed using Student's t-test or one-way analysis of variance (ANOVA) with Tukey's multiple comparison *post hoc* test. Statistical analysis of non-parametric data was performed using Kolmogorov-Smirnov chi-square tests. Significance was defined as $\alpha \leq 0.05$ and all p-values are reported with their respective data-sets. GraphPad Prism software v6.0 (GraphPad Software, La Jolla, CA) was used for all analyses.

Received: 5 March 2020; Accepted: 26 May 2020;
Published online: 17 June 2020

References

1. Catalano, V. *et al*. Tumor and its microenvironment: a synergistic interplay. *Seminars in cancer biology* **23**, 522–532, https://doi.org/10.1016/j.semcancer.2013.08.007 (2013).
2. Hanahan, D. & Coussens, L. M. Accessories to the crime: functions of cells recruited to the tumor microenvironment. *Cancer cell* **21**, 309–322, https://doi.org/10.1016/j.ccr.2012.02.022 (2012).
3. Pietras, K. & Östman, A. Hallmarks of cancer: Interactions with the tumor stroma. *Experimental Cell Research* **316**, 1324–1331, https://doi.org/10.1016/j.yexcr.2010.02.045 (2010).
4. Khoo, C. Y., Chai, X., Quek, R., Teo, M. C. C. & Goh, B. K. P. Systematic review of current prognostication systems for primary gastrointestinal stromal tumors. *European journal of surgical oncology: the journal of the European Society of Surgical Oncology and the British Association of Surgical Oncology* **44**, 388–394, https://doi.org/10.1016/j.ejso.2017.12.006 (2018).
5. Carreras-Torras, C. & Gay-Escoda, C. Techniques for early diagnosis of oral squamous cell carcinoma: Systematic review. *Med Oral Patol Oral Cir Bucal* **20**, e305–e315, https://doi.org/10.4317/medoral.20347 (2015).
6. Bremnes, R. M. *et al*. The role of tumor stroma in cancer progression and prognosis: emphasis on carcinoma-associated fibroblasts and non-small cell lung cancer. *Journal of thoracic oncology: official publication of the International Association for the Study of Lung Cancer* **6**, 209–217, https://doi.org/10.1097/JTO.0b013e3181f8a1bd (2011).
7. Valkenburg, K. C., de Groot, A. E. & Pienta, K. J. Targeting the tumour stroma to improve cancer therapy. *Nat Rev Clin Oncol* **15**, 366–381, https://doi.org/10.1038/s41571-018-0007-1 (2018).

8. Nurgali, K., Jagoe, R. T. & Abalo, R. Editorial: Adverse Effects of Cancer Chemotherapy: Anything New to Improve Tolerance and Reduce Sequelae? *Front Pharmacol* **9**, 245–245, https://doi.org/10.3389/fphar.2018.00245 (2018).
9. Schirrmacher, V. From chemotherapy to biological therapy: A review of novel concepts to reduce the side effects of systemic cancer treatment (Review). *Int J Oncol* **54**, 407–419, https://doi.org/10.3892/ijo.2018.4661 (2019).
10. Baker, E. L., Lu, J., Yu, D., Bonnecaze, R. T. & Zaman, M. H. Cancer Cell Stiffness: Integrated Roles of Three-Dimensional Matrix Stiffness and Transforming Potential. *Biophysical Journal* **99**, 2048–2057, https://doi.org/10.1016/j.bpj.2010.07.051 (2010).
11. Fenner, J. *et al*. Macroscopic Stiffness of Breast Tumors Predicts Metastasis. *Scientific Reports* **4**, 5512, https://doi.org/10.1038/srep05512 (2014).
12. Schrader, J. *et al*. Matrix Stiffness Modulates Proliferation, Chemotherapeutic Response and Dormancy in Hepatocellular Carcinoma Cells. *Hepatology (Baltimore, Md.)* **53**, 1192–1205, https://doi.org/10.1002/hep.24108 (2011).
13. Burke, K. & Brown, E. The Use of Second Harmonic Generation to Image the Extracellular Matrix During Tumor Progression. *IntraVital* **3**, e984509, https://doi.org/10.4161/21659087.2014.984509 (2014).
14. Cox, T. R. *et al*. LOX-mediated collagen crosslinking is responsible for fibrosis-enhanced metastasis. *Cancer research* **73**, 1721–1732, https://doi.org/10.1158/0008-5472.CAN-12-2233 (2013).
15. Lancaster, M. A. & Huch, M. Disease modelling in human organoids. *Dis Model Mech* **12**, dmm039347, https://doi.org/10.1242/dmm.039347 (2019).
16. Kang, N., Gores, G. J. & Shah, V. H. Hepatic stellate cells: partners in crime for liver metastases? *Hepatology* **54**, 707–713, https://doi.org/10.1002/hep.24384 (2011).
17. Devarasetty, M., Wang, E., Soker, S. & Skardal, A. Mesenchymal stem cells support growth and organization of host-liver colorectal-tumor organoids and possibly resistance to chemotherapy. *Biofabrication* **9**, 021002 (2017).
18. Skardal, A., Devarasetty, M., Rodman, C., Atala, A. & Soker, S. Liver-Tumor Hybrid Organoids for Modeling Tumor Growth and Drug Response *In Vitro*. *Annals of biomedical engineering*, https://doi.org/10.1007/s10439-015-1298-3 (2015).
19. Simian, M. & Bissell, M. J. Organoids: A historical perspective of thinking in three dimensions. *J. Cell Biol* **216**, 31–40, https://doi.org/10.1083/jcb.201610056 (2017).
20. Lancaster, M. A. & Knoblich, J. A. Organogenesis in a dish: Modeling development and disease using organoid technologies. *Science* **345**, 1247125, https://doi.org/10.1126/science.1247125 (2014).
21. Huch, M. & Koo, B. K. Modeling mouse and human development using organoid cultures. *Development (Cambridge, England)* **142**, 3113–3125, https://doi.org/10.1242/dev.118570 (2015).
22. Sung, J. H. *et al*. Recent Advances in Body-on-a-Chip Systems. *Anal Chem* **91**, 330–351, https://doi.org/10.1021/acs.analchem.8b05293 (2019).
23. Skardal, A. *et al*. Multi-tissue interactions in an integrated three-tissue organ-on-a-chip platform. *Scientific Reports* **7**, 8837, https://doi.org/10.1038/s41598-017-08879-x (2017).
24. Skardal, A., Shupe, T. & Atala, A. Organoid-on-a-chip and body-on-a-chip systems for drug screening and disease modeling. *Drug discovery today* **21**, 1399–1411, https://doi.org/10.1016/j.drudis.2016.07.003 (2016).
25. Riihimäki, M., Hemminki, A., Sundquist, J. & Hemminki, K. Patterns of metastasis in colon and rectal cancer. *Scientific reports* **6**, 29765–29765, https://doi.org/10.1038/srep29765 (2016).
26. Hernández-Morera, P., Castaño-González, I., Travieso-González, C. M., Mompeó-Corredera, B. & Ortega-Santana, F. Quantification and Statistical Analysis Methods for Vessel Wall Components from Stained Images with Masson's Trichrome. *Plos One* **11**, e0146954, https://doi.org/10.1371/journal.pone.0146954 (2016).
27. Schipke, J. *et al*. Assessment of cardiac fibrosis: a morphometric method comparison for collagen quantification. *Journal of applied physiology (Bethesda, Md.: 1985)* **122**, 1019–1030, https://doi.org/10.1152/japplphysiol.00987.2016 (2017).
28. Sannad, A. *et al*. Total Serum Protein Estimation and Its Correlation with Clinical and Histopathological Grading using Masson's Trichrome Stain in Patients of Oral Submucous Fibrosis. *Contemporary clinical dentistry* **8**, 286–292, https://doi.org/10.4103/ccd.ccd_95_17 (2017).
29. Bredfeldt, J. S. *et al*. Automated quantification of aligned collagen for human breast carcinoma prognosis. *Journal of Pathology Informatics* **5**, 28, https://doi.org/10.4103/2153-3539.139707 (2014).
30. Xu, L. *et al*. Human hepatic stellate cell lines, LX-1 and LX-2: new tools for analysis of hepatic fibrosis. *Gut.* **54**, 142–151, https://doi.org/10.1136/gut.2004.042127 (2005).
31. Shimizu, S. *et al*. *In vivo* and *in vitro* interactions between human colon carcinoma cells and hepatic stellate cells. *Japanese journal of cancer research: Gann* **91**, 1285–1295 (2000).
32. Rigamonti, C., Mazzocca, A., Cappadona, S., Carloni, V. & Pinzani, M. Human hepatic stellate cells (HSC) promote scattering and invasion of colon cancer cells. *Journal of Hepatology* **36**, 164, https://doi.org/10.1016/S0168-8278(02)80594-3 (2002).
33. Loh, C.-Y. *et al*. The E-Cadherin and N-Cadherin Switch in Epithelial-to-Mesenchymal Transition: Signaling, Therapeutic Implications, and Challenges. *Cells* **8**, 1118, https://doi.org/10.3390/cells8101118 (2019).
34. Araki, K. *et al*. E/N-cadherin switch mediates cancer progression via TGF-beta-induced epithelial-to-mesenchymal transition in extrahepatic cholangiocarcinoma. *British journal of cancer* **105**, 1885–1893, https://doi.org/10.1038/bjc.2011.452 (2011).
35. Zhu, Q. C., Gao, R. Y., Wu, W. & Qin, H. L. Epithelial-mesenchymal transition and its role in the pathogenesis of colorectal cancer. *Asian Pacific journal of cancer prevention: APJCP* **14**, 2689–2698 (2013).
36. Amann, T. *et al*. Activated hepatic stellate cells promote tumorigenicity of hepatocellular carcinoma. *Cancer science* **100**, 646–653, https://doi.org/10.1111/j.1349-7006.2009.01087.x (2009).
37. Basu, S., Haase, G. & Ben-Ze'ev, A. Wnt signaling in cancer stem cells and colon cancer metastasis. *F1000Research* 5, F1000 Faculty Rev-1699, https://doi.org/10.12688/f1000research.7579.1 (2016).
38. Sulzmaier, F. J., Jean, C. & Schlaepfer, D. D. FAK in cancer: mechanistic findings and clinical applications. *Nat. Rev. Cancer* **14**, 598–610, https://doi.org/10.1038/nrc3792 (2014).
39. Royce, M. E. *et al*. Colorectal cancer: chemotherapy treatment overview. *Oncology (Williston Park, N.Y.)* **14**, 40–46 (2000).
40. Gustavsson, B. *et al*. A review of the evolution of systemic chemotherapy in the management of colorectal cancer. *Clinical colorectal cancer* **14**, 1–10, https://doi.org/10.1016/j.clcc.2014.11.002 (2015).
41. Aljubran, A. *et al*. Efficacy of Regorafenib in Metastatic Colorectal Cancer: A Multi-institutional Retrospective Study. *Clin Med Insights Oncol* **13**, 1179554918825447–1179554918825447, https://doi.org/10.1177/1179554918825447 (2019).
42. Botchkina, I. L. *et al*. Phenotypic subpopulations of metastatic colon cancer stem cells: genomic analysis. *Cancer genomics & proteomics* **6**, 19–29 (2009).
43. Chamie, K. *et al*. Recurrence of high-risk bladder cancer: a population-based analysis. *Cancer* **119**, 3219–3227, https://doi.org/10.1002/cncr.28147 (2013).
44. Al-Kharusi, M. R. A. *et al*. LGR5 promotes survival in human colorectal adenoma cells and is upregulated by PGE2: implications for targeting adenoma stem cells with NSAIDs. *Carcinogenesis* **34**, 1150–1157, https://doi.org/10.1093/carcin/bgt020 (2013).
45. Su, S. *et al*. Lgr5 Methylation in Cancer Stem Cell Differentiation and Prognosis-Prediction in Colorectal Cancer. *Plos One* **10**, e0143513, https://doi.org/10.1371/journal.pone.0143513 (2015).
46. Matsusue, R. *et al*. Hepatic stellate cells promote liver metastasis of colon cancer cells by the action of SDF-1/CXCR4 axis. *Ann Surg Oncol* **16**, 2645–2653, https://doi.org/10.1245/s10434-009-0599-x (2009).
47. Devarasetty, M., Skardal, A., Cowdrick, K., Marini, F. & Soker, S. Bioengineered Submucosal Organoids for *In Vitro* Modeling of Colorectal Cancer. *Tissue engineering. Part A* **23**, 1026–1041, https://doi.org/10.1089/ten.tea.2017.0397 (2017).

Acknowledgements
We thank Dr. Scott Friedman from the Icahn School of Medicine at Mount Sinai, New York, for providing LX2 cells. The authors acknowledge funding through the NIH NCI grant R33CA202822. The authors wish to acknowledge the support of the Wake Forest Baptist Comprehensive Cancer Center Tumor Tissue and Pathology Shared Resource supported by the National Cancer Institute's Cancer Center Support Grant award number P30CA012197.

Author contributions
M.D., S.H., A.S. and S.S. designed experiments. M.D. performed all *in vitro* experiments. M.D., S.H. and A.D. performed all *in vivo* experiments. M.D., A.D. and E.S. performed immunohistochemical staining and imaging. M.D. designed and performed all digital segmentation analysis. M.D. designed all figures. M.D., S.H. and S.S. prepared manuscript text. All authors reviewed data and text.

Competing interests
The authors declare no competing interests.

Additional information
Supplementary information is available for this paper at https://doi.org/10.1038/s41598-020-66785-1.

Correspondence and requests for materials should be addressed to S.S.

Reprints and permissions information is available at www.nature.com/reprints.

Publisher's note Springer Nature remains neutral with regard to jurisdictional claims in published maps and institutional affiliations.